

Scanning X-ray imaging with small-angle scattering contrast

Aurelien Gourrier,^a Wolfgang Wagermaier,^a Manfred Burghammer,^b Donna Lammie,^c Himadri S. Gupta,^a Peter Fratzl,^a Christian Riekkel,^b Tim J. Wess^c and Oskar Paris^{a*}

^aDepartment of Biomaterials, Max-Planck Institute of Colloids and Interfaces, Potsdam, Germany, ^bEuropean Synchrotron Radiation Facility, Grenoble, France, and ^cSchool of Optometry and Vision Science, Cardiff University, UK. Correspondence e-mail: paris@mpikg.mpg.de

An X-ray scanning imaging technique using the integrated intensity of the small-angle X-ray scattering (SAXS) signal is presented. The technique is based on two-dimensional scanning of a thin sample section with an X-ray microbeam, collecting SAXS patterns at every scanning step using a two-dimensional detector. The integrated intensity within pre-defined regions of interest of the SAXS patterns is used to image bulk nanostructural features in the specimen with micrometre resolution which are usually not accessible by other methods such as light microscopy or scanning electron microscopy. The possibilities and limitations of the method are discussed with particular emphasis on the sources of contrast in the SAXS region for three biological specimens: cortical bone, eggshell and hair. Two main sources of image contrast are identified in the form of orientation effects for strongly anisotropic systems like cortical bone and differences in the local volume fraction of the scattering entities in eggshell. Moreover, other parameters than the integrated intensity can be quantitatively deduced from the SAXS patterns, for instance, the mean thickness of mineral platelets in bone or the strain distributions in a hair deformed plastically by microindentation.

© 2007 International Union of Crystallography
Printed in Singapore – all rights reserved

1. Introduction

Structural studies of complex materials generally imply the consideration of features over a large range of sizes. This is particularly true for hierarchical structures found in biological materials, for which outstanding physical properties are thought to be achieved by optimization of the structure at all levels (Weiner *et al.*, 1999; Aizenberg *et al.*, 2005). In this respect, many techniques spanning several orders of magnitude in length scales are generally required to relate the functional properties to the hierarchical structure. In addition, the precise characterization of heterogeneous samples entails some degree of mapping in order to measure physical parameters of interest within different regions of the sample. For this purpose, a large number of imaging techniques are available, either in full-field mode, such as light microscopy or transmission electron microscopy (TEM), or in scanning mode, as for instance in scanning electron microscopy (SEM), atomic force microscopy, Raman or infra-red (IR) spectroscopy imaging.

The need for a better characterization of bulk samples on the sub-micrometre scale often leads to complementary studies using X-ray, electron or neutron scattering techniques. These provide details on the atomic and molecular order as well as average shape, size and orientation of nanometre-sized heterogeneities within the region probed by the beam. The combination of these techniques with scanning possibilities to enhance spatial resolution has long been used in SEM (*e.g.* electron back-scatter diffraction) and TEM, since the beam size can readily be tuned. However, the use of hard X-rays

as a probe for scanning imaging using scattering as a contrast source is more recent. It is strongly related to the high brilliance of third-generation synchrotron-radiation sources and to the progress in the development of X-ray optics, which allows beam sizes in the sub-micrometre range with low divergence to be obtained (Riekkel, 2000).

A powerful approach recently developed is to use scanning small-angle and/or wide-angle X-ray scattering (SAXS/WAXS) to map local structural features in heterogeneous systems (Fratzl *et al.*, 1997; Rinnerthaler *et al.*, 1999; Riekkel, 2000; Paris *et al.*, 2000; Fratzl, 2003). The basic principle relies on using an intense X-ray beam of small dimension to scan a thin section of the sample with steps of the order of the beam size. This enables the reconstruction of images where each pixel is a representation of the local value of a nanostructural parameter obtained from the analysis of the scattering pattern. The lateral resolution of this image is thus given by the beam size to a first approximation. However, this method relies on a systematic analysis of the scattering patterns, which becomes rather tedious as the number of frames increases by orders of magnitude due to smaller beam sizes and faster detector read-out time, allowing larger areas to be covered.

The aim of this work is to present an alternative and yet complementary path which consists of imaging the integrated SAXS intensity. We show that this provides valuable preliminary information about the local distribution of nanostructural features in materials without previous knowledge of the structure. Examples of SAXS imaging from three biological materials, bone, eggshell and hair, are discussed. We show that the contrast in the SAXS images may be

qualitatively related to specific parameters such as orientation or volume fraction of nanoscopic particles. Even though it is qualitative in nature, such immediate information is essential to guide more detailed analysis, and, hence, marks the first step towards quantitative SAXS imaging.

2. Experimental

The thin bone sections of 3–4 μm thickness used in this study originate from a femoral midshaft sample of a healthy human female and were prepared as described in a previous study (Wagermaier *et al.*, 2006). An eggshell section of 110 μm thickness was prepared following a well established procedure (Lammie *et al.*, 2006). A human hair sample of approximately 85 μm in diameter was used without any chemical treatment and deformed using a micro-indentation technique using a force of 1000 mN, at a rate of 100 mN s⁻¹ for 10 s, following a protocol established in previous experiments with synthetic polymer fibres (Gourrier *et al.*, 2002, 2005, 2006; García-Gutiérrez *et al.*, 2004; Riekel *et al.*, 2003).

The experiments were carried out at the microfocus beamline (ID13) of the European Synchrotron Radiation Facility (ESRF). A monochromatic beam of wavelength $\lambda = 0.0976$ nm ($E = 12.78$ keV) was obtained using an Si (111) double-crystal monochromator and reduced in size to approximately 1×1 μm using a set of Kirkpatrick–Baez (KB) mirrors. The specimens were visualized by an on-axis optical microscope, which could be remotely interchanged with the SAXS/WAXS detector. Thus, the scanning regions could be defined within a calibrated setup, and for each scan the corresponding light microscopy image was available. A 16-bit charge coupled device detector with fibre-optic taper (MARCCD, Mar Inc., USA) with a

130 mm diameter X-ray converter screen and 2048×2048 pixels of 64.45×64.45 μm was used for SAXS/WAXS data collection. Scans were carried out at constant monitor flux using a small ionization chamber placed in front of the sample with the SAXS guard aperture mounted on the outlet of the ionization chamber. Typical measurement times for a single frame were of the order of 10 s. The sample-to-detector distance and the detector tilt and centre were calibrated using a silver behenate standard (Blanton *et al.*, 1995). All SAXS data were corrected for parasitic scattering by taking into account the transmission measured using a photodiode with the same scan parameters as for the collection of SAXS/WAXS data.

Data were first reduced and analysed online using a specific library which is being written by one of the authors (M. Burghammer) in the *Python* programming language in combination with the *FIT2D* software package (Hammersley, 1997). The final images presented in this paper were obtained using a dedicated SAXS analysis library written in *Python* by one of the authors (A. Gourrier). In particular, the imaging part of this code strongly relies on the *Matplotlib* library (Barret *et al.*, 2005).

3. Imaging experiments

In the following sections, the integrated intensity of the SAXS signal in the plane of the detector refers to the scalar quantity

$$I = \int_{q_{\min}}^{q_{\max}} \int_{\chi_1}^{\chi_2} I(q, \chi) q^2 dq d\chi, \quad (1)$$

where $q = (4\pi/\lambda)\sin\theta$ is the length of the scattering vector, 2θ being the scattering angle measured in radial coordinates on the two-dimensional detector, and χ is the azimuthal angle. Adapting q_{\min} and q_{\max} and the range of angular integration (χ) allows a specific region of interest to be imaged. In the experiments described, a q range of $q_{\min} = 0.1$, $q_{\max} = 3$ nm⁻¹ was selected and the angular integration was performed over 2π .

It is well known from the SAXS theory that the integrated intensity for a two-phase system with uniform electron density for each phase can be expressed in the following way (Glatter & Kratky, 1982):

$$\begin{aligned} \tilde{I} &= \int I(\mathbf{q}) d^3q = \int_0^\infty q^2 dq \int_0^\pi \sin\psi d\psi \int_0^{2\pi} I(q, \psi, \chi) d\chi \\ &= 2\pi^2 \varphi_1 \varphi_2 (\Delta\rho)^2, \end{aligned} \quad (2)$$

where φ_1 and $\varphi_2 = 1 - \varphi_1$ are the volume fractions of the two phases and $\Delta\rho = \rho_1 - \rho_2$ is the mean electron density difference between those two phases. As long as the SAXS signal is spherically isotropic, equations (1) and (2) are closely related, and the integrated SAXS intensity is proportional to the volume fraction of the two phases and to the scattering contrast. This is not true in the case of anisotropic scattering objects, since the scattering pattern recorded on the two-dimensional detector represents the intersection of the three-dimensional SAXS signal with the Ewald sphere. In such a case, unless the full three-dimensional scattering signal is collected by rotating the sample, the measured intensity will also depend on the orientation of the anisotropic scattering objects.

3.1. Bone section

The on-axis light microscopy image of the bone specimen is shown in Fig. 1a. The lamellar structure around the central hole of the osteon reflects the changing orientation of the collagen fibres within the lamellae. Although it is generally better visualized with polarized light (Ascenzi *et al.*, 2003), it is also clearly seen on the optical image,

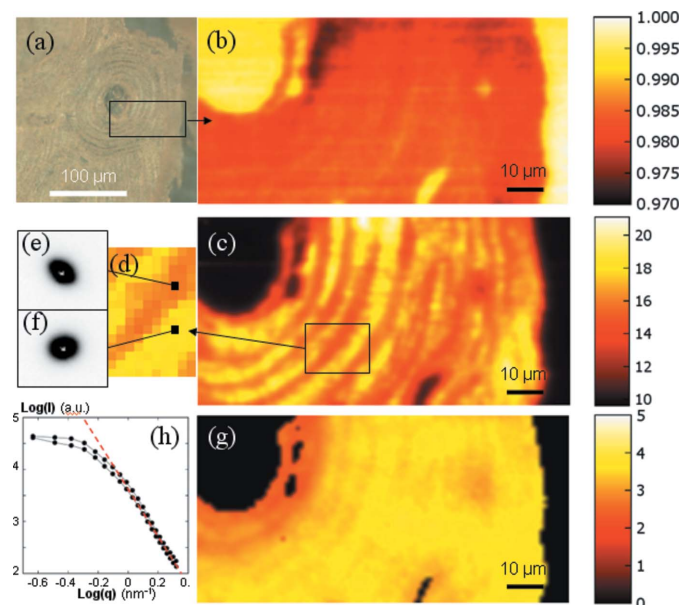


Figure 1 (a) Optical microscopy images of a 5 μm thick human bone section taken in the dense cortical part of the femoral midshaft of a healthy human female; (b) X-ray transmission scan of the region indicated by the box in (a), obtained using a 1 μm diameter beam with 1 μm scan steps in both directions; (c) image of the SAXS intensity (arbitrary units) according to equation (1) using the same scan parameters; (d) magnified region of the box in (c); (e, f) individual two-dimensional SAXS patterns from (d); (g) image of the mineral platelet thickness T (in nm) using the same scan parameters as in (b) and (c); (h) azimuthally averaged intensity profiles from the scattering patterns (e) and (f). The red dotted line shows a -4 slope in the double-logarithmic representation in accordance with Porod's law.

probably due to different grinding and polishing effects during sample preparation on regions with different mechanical properties. A transmission scan of a region of interest of the sample (box in Fig. 1a) was recorded in 100 horizontal and 50 vertical steps of 1 μm in both directions (Fig. 1b), followed by a scan acquisition of SAXS data with the same parameters. Thus, the 100 \times 50 μm scan region was fully covered with the best achievable resolution of 1 μm in direct space. The main features that can be clearly distinguished in the transmission scan are the Haversian canal (upper left hole) and lacunae. The lamellar structure of the osteon observed in the light microscopy image is only weakly apparent in the transmission image. On the other hand, the image of the total scattering intensity (Fig. 1c) clearly reveals alternating concentric rings strongly reflecting the lamellar structure also seen in the light micrograph. These rings are only weakly perturbed around the lacunae and tend to disappear close to the sample edge. The lower intensity rings, in a darker colour on the picture, also seem to be thinner than those of higher intensity (brighter on the picture) by a factor of ~ 0.5 on average in the best defined regions. This is emphasized in Fig. 1d, which shows an enlarged region of the previous image (box in Fig. 1c). Details of the two-dimensional scattering patterns at two points taken in one of the darker and brighter rings are shown respectively in Fig. 1e and f.

In order to understand the origin of the contrast in this image, it is recalled that bone can be described by a two-phase model of mineral platelets, with given size and orientation distributions, embedded in an organic matrix of collagen (Currey, 2002; Fratzl *et al.*, 1991, 1992). The observed two-dimensional SAXS signal is anisotropic, reflecting the shape and orientation distribution of the mineral particles (Fratzl *et al.*, 1996). Qualitatively, an iso-intensity contour from a distribution of plate-like particles can be approximated by a prolate ellipsoid, and its planar intersection gives rise to elliptical two-dimensional SAXS patterns. Hence, both the local average crystallite size and the preferred orientation within the bone volume probed by the beam may contribute to the SAXS contrast seen in Fig. 1c (Fratzl *et al.*, 1997).

To evaluate possible changes in particle size, a scalar parameter which is independent of the shape and distribution of the mineral particles was calculated at each scan position following the procedure first established by Porod (1951, 1952):

$$T = \frac{4}{\pi P} \int_0^{\infty} I(q)q^2 dq = 4 \frac{\phi_1 \phi_2}{\sigma}, \quad (3)$$

where P is the Porod constant derived from Porod's law at large values of q (Glatter & Kratky, 1982) and σ is the total interface per unit volume between the two phases. In the case of bone, Fratzl *et al.* (1991, 1992, 1996) showed that this so-called T parameter can be related to the average mineral platelet thickness. The image of the T parameter (Fig. 1g) shows values of $\sim 3\text{--}4$ nm, which agrees well with the literature for mature bone (*e.g.* Fratzl *et al.*, 1992). Similar ring-like features in the intensity image can also be observed, although the contrast is considerably weaker. Interestingly, lower values can be found at the innermost rings close to the Haversian channel (Fig. 1g) which are not reflected in the other images (Fig. 1b, c). Since the changes in the mineral density (transmission) and particle dimensions (T parameter) are much weaker than those seen in the intensity image in Fig. 1c, we conclude that the contrast in the SAXS intensity image mostly results from a change in local orientation of the crystallites. Moreover, the direction of the short axis is circumferential around the central hole, which has been observed in earlier work with lower position resolution (Paris *et al.*, 2000). Recent studies confirmed that the collagen fibre orientation changes between adjacent lamellae, suggesting a twisted plywood model (Wagermaier *et al.*, 2006). Our results are therefore consistent with this model.

3.2. Eggshell section

Eggshell is a biomineral composite exhibiting an intimate relationship between calcitic and protein deposition that directs the overall stratigraphy of the shell layers. A region of interest was selected on the mammillary layer of the eggshell section based on the online optical microscope image (box in Fig. 2a). This layer is responsible for the initial spherulitic growth phase of eggshell on a collagenous membrane. SAXS data were collected in 65 horizontal and 20 vertical steps of 2 and 5 μm , respectively, covering a total area of 130 \times 100 μm . The transmission scan obtained using the same scan parameters is shown in Fig. 2b. It appears higher in the mammillary membrane region and darker in the mineralized part, *i.e.* on the left and right of the image, respectively. The image of the integrated SAXS intensity (Fig. 2c) reveals strikingly different features in the form of three very intense microscopic focal discs stacked vertically. The lowest is not as clearly defined as the upper two and its surrounding region shows some diffuse features. The average diameter of the two best defined discs is $\sim 36\text{--}42$ μm . Furthermore, the

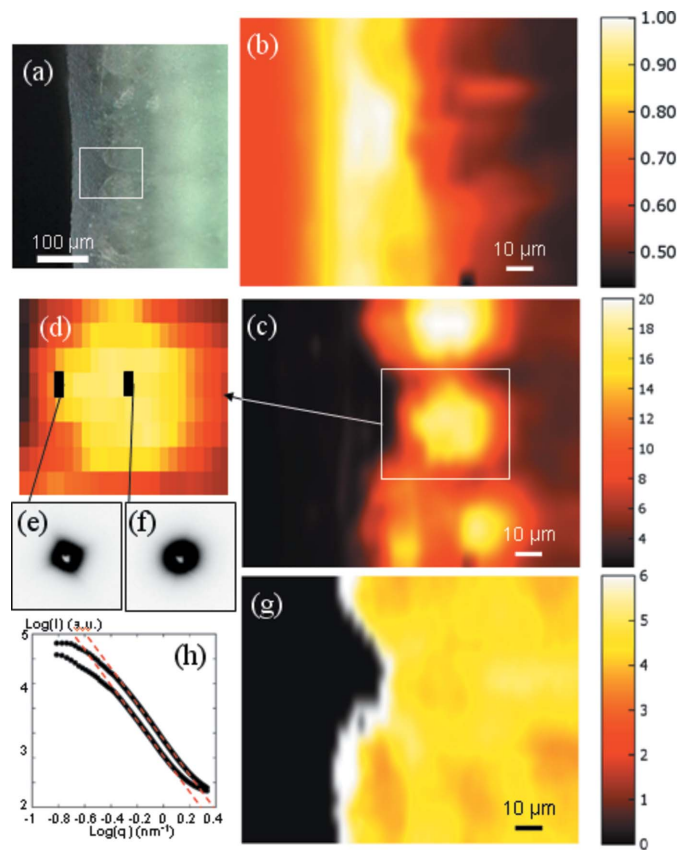


Figure 2 (a) Optical microscopy images of the inner surface of a 110 μm thick eggshell section showing the membrane on the left and mammillary spherulitic layer on the right; (b) X-ray transmission image of the region indicated by the box in (a) obtained using a 1 μm diameter beam with a scan step of 2 μm horizontally and 5 μm vertically; (c) integrated SAXS intensity (arbitrary units) of the same region; (d) details for the central disc (box in c); (e, f) individual SAXS patterns taken, respectively, at the border and the centre of the disc; (g) image of the T parameter (in nm) using the same scan parameters as in (b) and (c); (h) azimuthally averaged intensity profiles from the scattering patterns (e) and (f). The red dotted line shows a -4 slope in the double-logarithmic representation in accordance with Porod's law.

intensity on the right of the disc is a factor of two higher than on the left-hand side.

By comparison with the optical microscopy image of Fig. 2a, the upper and lower discs appear at the positions of the nucleating knobs, close to the interface between the organic membrane layer (left) and mineral part (right). These are known to form as spherulites and initiate shell growth during the mineralization process (Arias *et al.*, 1992; Fernandez *et al.*, 2001), and are of composite nature comprising mineral and organic phases. Since the discs are about 40 μm in diameter, which is much less than the section thickness (110 μm), and the results of the scattering data are a projection of volume information, the central feature is probably simply another nucleating centre formed below the surface under examination. Unlike the case of bone described previously, the SAXS patterns taken in the inner part of the disc (Fig. 2f) differ strongly in shape (or symmetry) compared to those taken in the outer part (Fig. 2e). The former appear to be nearly circular or slightly elliptical, while the latter are polygonal (four-sided in the pattern shown in Fig. 2e, sometimes also showing sixfold symmetry). An important observation is the fact that the intensity ratio between the centre and the outer part of the discs observed in the SAXS image of the eggshell section corresponds to a factor of $\sim 4\text{--}8$ (Fig. 2c). It should be noted that the intensity difference between alternating dark and lighter layers in bone differed only by a factor of two at most (Fig. 1c).

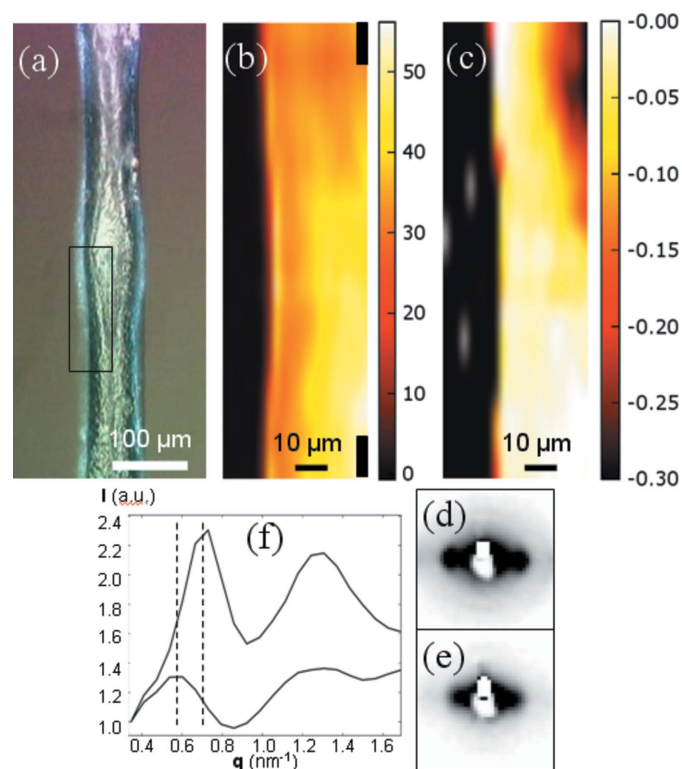


Figure 3
(a) Optical microscopy image of an 85 μm diameter hair deformed by microindentation using a load of 1000 mN at 100 mN s $^{-1}$ for 10 s; (b) integrated SAXS intensity of the same region obtained using a 1 μm diameter beam with a scan step of 2 μm horizontally and 8 μm vertically; (c) image of the percentage shift in the peak position corresponding to the interfibrillar distance using the same scan parameters; (d, e) individual SAXS patterns taken, respectively, in an undeformed part of the fibre and in the vicinity of the deformed region indicated in (b) by upper and lower black pixels; (f) radial intensity profiles of the scattering patterns shown in (d) and (e), respectively, by the upper and lower curves, corrected for the scattering of the amorphous background; dotted lines indicate the peak shift to lower q values in the deformed region.

Following similar considerations as in the case of bone, the contrast observed in the integrated scattering intensity images can originate from variations in equation (2) either of the volume fractions of the two phases and/or the scattering contrast, as well as from differences in orientation of the scattering objects. Since the anisotropy is rather weak in the case of the eggshell (either moderate elliptical, fourfold or sixfold symmetry), a change in the orientation of an anisotropic three-dimensional SAXS signal alone cannot account for more than a factor of two in the scattering intensity. Since the eggshell is known to consist of $\sim 95\%$ mineral and about 5% proteins overall, the factor of $\sim 4\text{--}8$ in the difference of integrated intensity between the nucleating knob and the remaining mineralized layer may therefore be accounted for by a decrease in the volume fraction of the organic content from the centre to the outside of the knob, as also observed in other studies (*e.g.* Arias *et al.*, 1992; Fraser *et al.*, 1998). The T parameter calculated in the same way as for bone and shown in Fig. 2g is constant throughout the mineralized layer with a value of $\sim 4\text{--}5$ nm. The local surface-to-volume ratio between the two phases therefore remains unchanged throughout the mineralized part of the sample [equation (3)].

3.3. Hair specimen

A region of interest covering the lower quarter of the indentation zone of the hair (box in Fig. 3a) was scanned in 22 horizontal and 17 vertical steps of 2 and 8 μm , respectively, spanning a total area of 44 \times 136 μm . Owing to the very low absorption of this pure polymeric material, no transmission scan was recorded during the experiment. The image of the integrated intensity of the SAXS signal is shown in Fig. 3b. In the undeformed part, the intensity increases progressively from the outer part of the fibre towards the fibre axis as observed in the lower part of this image. This is due to the increase in scattering volume resulting from the convolution of the beam profile and the local fibre thickness (Gourrier *et al.*, 2006; Riekel, 2000; Paris *et al.*, 2000). In the indentation zone, this is no longer true, and the scattering intensity remains almost constant across the fibre. A reasonable explanation for this observation is that the material expands laterally under the pressure of the indenter during the deformation process, which leads to a reduced thickness in the centre of the indentation. This is a general effect observed in all previous experiments of this type performed on polymer fibres (Gourrier *et al.*, 2002, 2005, 2006; García-Gutiérrez *et al.*, 2004; Riekel *et al.*, 2003). The integrated SAXS intensity image therefore yields no additional structural information relative to the effect of the deformation process. This is apparent when comparing the SAXS patterns taken from undeformed part with the centre of the indentation (Fig. 3d and e, respectively) which reveals no immediate structural changes.

In such a case, a more detailed analysis has to be carried out. This can be done, *e.g.* by considering the strong interference peaks in the SAXS pattern indicating a high degree of ordering on the nanometre scale. The best-known model developed to date is that of Briki *et al.* (1998) based on a distorted hexagonal arrangement of keratin nanofibrils. Radial profiles were calculated by integration of the intensity within an azimuthal segment of 3 $^\circ$ about the equatorial direction. A background proportional to $q^{-2.3}$ was subtracted to account for the amorphous interfibrillar matrix following the method described in detail by Briki *et al.* Finally, the interfibrillar distance was extracted by fitting the first peak of the equatorial profile with a Gaussian function. This allowed the reconstruction of an image showing the relative shift in peak position at each scan point (Fig. 3c). This image clearly reveals an increase in interfibrillar distance in the indentation zone, which indicates that the stresses induced in the

deformation process lead to an expansion of the interfibrillar matrix in the direction normal to the direction of applied load. Thus, Fig. 3c represents a direct image of the local strains in the indented fibre.

4. Conclusion

The improvements in scanning X-ray scattering techniques currently lead to the acquisition of several thousand scattering patterns for a single specimen which cannot be analysed manually. Thus, simple and robust structural parameters have to be defined which can be reliably deduced from the raw data in an automated way. Investigating three biomaterials, namely bone, eggshell and hair, we have shown that imaging using the integrated SAXS intensity can provide valuable insight into the structure of materials on the nanometre scale. This is a very straightforward step requiring little or no user input and can therefore easily be carried out online during data acquisition, like in other imaging techniques. In addition, these images can be combined with data from other imaging techniques to allow a qualitative interpretation. The orientation of the mineral platelets in osteonal bone, for instance, appears to be an important source of contrast, while in eggshell the image contrast can largely be attributed to local changes in the volume fractions of proteins. Quantitative structural parameters of interest can be imaged, providing a well established model is available for high-throughput data reduction and analysis, such as the average particle thickness for bone or the local strain in deformed hair, although this approach is clearly less straightforward. Adapted software development for large data set analysis is therefore another key issue for the further development of this method towards quantitative SAXS imaging. It is likely that the technique will greatly benefit from many ongoing developments in the synchrotron community. Scanning SAXS imaging could in turn provide a powerful tool for studies of weakly ordered structures for a wide range of materials.

We acknowledge beamtime from the ESRF in the framework of the long-term project SC-1579 'Scanning diffractometry of hierarchical biological tissues'. Financial support from the Max Planck Society is also gratefully acknowledged. We thank Gerda Dinst (Ludwig Boltzmann Institut of Osteology, Vienna) for bone sample preparation and Annemarie Martins (Max Planck Institute of Colloids and Interfaces) for eggshell sample preparation. A. Gourrier would also like to thank Richard Davies (ESRF) for valuable discussions regarding software development.

References

- Aizenberg, J., Weaver, J. C., Thanawala, M. S., Sundar, V. C., Morse, D. E. & Fratzl, P. (2005). *Science*, **309**, 275–278.
- Arias, J. L., Carrino, D. A., Fernandez, M. S., Rodriguez, J. P., Denis, J. E. & Caplan, A. I. (1992). *Biochem. Biophys.* **298**, 293–302.
- Ascenzi, M., Ascenzi, A., Benvenuti, A., Burghammer, M., Panzavolta, S. & Bigi, A. (2003). *J. Struct. Biol.* **141**, 22–33.
- Barret, P., Hunter, J. D. & Greenfield, P. (2005). *Matplotlib – A Portable Python Plotting Package*. In *Proceedings from the Astronomical Data Analysis Software & Systems XIV Conference*. San Francisco: Astronomical Society of the Pacific.
- Blanton, T. N., Huang, T. C., Toraya, H., Hubbard, C. R., Robie, S. B., Louër, D., Göbel, H. E., Will, G., Gilles, R. & Raftery, T. (1995). *Powder Diff.* **10**, 91–95.
- Briki, F., Busson, B. & Doucet, J. (1998). *Biochim. Biophys. Acta*, **1429**, 57–68.
- Currey, J. D. (2002). *Bones: Structure and Mechanics*. Princeton, NJ: Princeton University Press.
- Fernandez, M. S., Moya, M., Lopez, L. & Arias, J. L. (2001). *Matrix Biol.* **18**, 793–803.
- Fraser, A. C., Bain, M. M. & Solomon, S. E. (1998). *Br. Poult. Sci.* **39**, 225–228.
- Fratzl, P. (2003). *J. Appl. Cryst.* **36**, 397–404.
- Fratzl, P., Fratzl-Zelman, N., Klaushofer, K., Vogl, G. & Koller, K. (1991). *Calcif. Tissue Int.* **48**, 407–413.
- Fratzl, P., Groschner, M., Vogl, G., Plenk, H. Jr, Eschberger, J., Fratzl-Zelman, N., Koller, K. & Klaushofer, K. (1992). *J. Bone Miner. Res.* **7**, 329–334.
- Fratzl, P., Jakob, H. F., Rinnerthaler, S., Roschger, P. & Klaushofer, K. (1997). *J. Appl. Cryst.* **30**, 765–769.
- Fratzl, P., Schreiber, S. & Klaushofer, K. (1996). *Connect. Tissue Res.* **34**, 247–25.
- García-Gutiérrez, M. C., Gourrier, A. & Riekkel, C. (2004). *J. Macromol. Sci. B*, **43**, 267–277.
- Glatter, O. & Kratky, O. (1982). Editors. *Small-Angle X-ray Scattering*. New York: Academic Press.
- Gourrier, A., García-Gutiérrez, M. C. & Riekkel, C. (2002). *Macromolecules*, **35**, 8072–8077.
- Gourrier, A., García-Gutiérrez, M. C. & Riekkel, C. (2005). *Macromolecules*, **38**, 3838–3844.
- Gourrier, A., García-Gutiérrez, M. C. & Riekkel, C. (2006). *Philos. Mag.* **86**, 5753–5767.
- Hammersley, A. P. (1997). ESRF Internal Report No. ESRF97, HA02T. European Synchrotron Radiation Facility, Grenoble, France.
- Lammie, D., Bain, M. M., Salomon, S. E. & Wess, T. J. (2006). *J. Bionic Eng.* **3**, 11–18.
- Paris, O., Zizak, I., Lichtenegger, H., Roschger, P., Klaushofer, K. & Fratzl, P. (2000). *Cell. Mol. Biol.* **46**, 993–1004.
- Porod, G. (1951). *Kolloid Z.* **124**, 83–113.
- Porod, G. (1952). *Kolloid Z.* **125**, 51–57.
- Riekkel, C. (2000). *Rep. Prog. Phys.* **63**, 233–262.
- Riekkel, C., García-Gutiérrez, M. C., Gourrier, A. & Roth, S. V. (2003). *Anal. Bioanal. Chem.* **376**, 594–601.
- Rinnerthaler, S., Roschger, P., Jakob, H. F., Nader, A., Klaushofer, K. & Fratzl, P. (1999). *Calc. Tissue Int.* **64**, 422–429.
- Wagermaier, W., Gupta, H. S., Gourrier, A., Burghammer, M., Roschger, P. & Fratzl, P. (2006). *Biointerphases*, **1**, 1–5.
- Weiner, S., Traub, W. & Wagner, H. (1999). *J. Struct. Biol.* **126**, 241–255.